Sensitivity analysis for high-contrast missions with segmented telescopes

Lucie Leboulleux, Jean-François Sauvage, Laurent Pueyo, Thierry Fusco, Rémi Soummer, Mamadou N'Diaye, Kathryn St.Laurent

Sensitivity analysis for high-contrast missions with segmented telescopes

Lucie Leboulleux[abc], Jean-François Sauvage[bc], Laurent Pueyo[a], Thierry Fusco[bc], Rémi Soummer[a], Mamadou N'Diaye[d], Kathryn St.Laurent[a]

[a] Space Telescope Science Institute, 3700 San Martin Drive, Baltimore, MD 21218, USA
[b] Aix Marseille Université, CNRS, LAM (Laboratoire d´Astrophysique de Marseille) UMR 7326, 13388, Marseille, France
[c] Office National d´Etudes et de Recherches Aérospatiales, 29 Avenue de la Division Leclerc, 92320 Châtillon, France
[d] Observatoire de Nice Côte d´Azur, Boulevard de l´Observatoire, 06304 Nice, France

ABSTRACT

Segmented telescopes enable large-aperture space telescopes for the direct imaging and spectroscopy of habitable worlds. However, the increased complexity of their aperture geometry, due to their central obstruction, support structures, and segment gaps, makes high-contrast imaging very challenging.
In this context, we present an analytical model that will enable to establish a comprehensive error budget to evaluate the constraints on the segments and the influence of the error terms on the final image and contrast. Indeed, the target contrast of 10^{10} to image Earth-like planets requires drastic conditions, both in term of segment alignment and telescope stability. Despite space telescopes evolving in a more friendly environment than ground-based telescopes, remaining vibrations and resonant modes on the segments can still deteriorate the contrast.
In this communication, we develop and validate the analytical model, and compare its outputs to images issued from end-to-end simulations.

Keywords: Segmented telescope, cophasing, exoplanet, high-contrast imaging, error budget

1. INTRODUCTION

The next generation of space telescopes for direct imaging and spectroscopy of exoplanets includes telescopes with a monolithic mirror, such as the Wide Field Infrared Survey Telescope (WFIRST)[1] and studies for telescopes with segmented primary mirrors, such as the Large Ultra-Violet Optical Infrared (LUVOIR) telescope[2,3] or the Habitable Exoplanet Imaging Mission (HabEx).[4] Even current and future ground-based telescopes have segmented apertures, such as the Keck telescopes[5,6] or the coming Extremely Large Telescopes (ELTs).[7–10] Unfortunately, the increased complexity of their aperture geometry, due to their central obstruction, support structures, and segment gaps, makes high-contrast imaging very challenging.
Indeed, to observe a habitable world, two constraints have to be respected. First, in a planetary system with a probable Earth-like planet, the ratio between the star photon flux and the planet photon flux, which is called the contrast, is higher than 10^{10}. Secondly, the angular separation between the star and the planet is smaller than 0.1 arcsec. Therefore, the region of interest is restricted to a so-called dark hole, a region centered on the star with a very high star-to-planet contrast. These two goals, the contrast and the angular separation, are extremely challenging to achieve, mainly in a segmented pupil configuration, which generates huge diffraction effects.
This performance is still far from being reached, since the best contrast achieved in laboratories corresponds to a few 10^9, obtained on the High-Contrast Imaging Testbed (HCIT) with a circular aperture.[11] A contrast of a few 10^8 was also reached on the Très Haute Dynamique (THD) bench below 0.5 arcsec,[12,13] which would allow

Further author information, send correspondence to Lucie Leboulleux: E-mail: leboulleux@stsci.edu, Telephone: 1 410 338 2881

the detection of young exo-Jupiters. But since this performance is reached on a clear aperture, the desired 10^{10} is still far from being achieved, particularly with segmented apertures.
To get a sufficient contrast stability, the studies for the chosen optical systems need to be completed with an error budget. Since numerous factors can degrade the performance of the system and since the objective is extremely challenging, a comprehensive error budget is essential in order to make the right decisions early enough in the system design process. The most traditional method for tolerancing is based on multiple end-to-end propagation simulations of the system.[14] At each iteration, an aberration or a group of aberrations is applied to a segment or a group of segments and propagated through the simulated optical system. This method is extremely time-consuming and is both pupil- and system-dependant.
We propose an alternative method, faster and adaptable to all segmented pupils, such as the James Webb Space Telescope (JWST),[15,16] the ELTs,[7–10] the HabEx mission,[4] or the LUVOIR telescope.[2,3] This new method is based on an analytical model to directly express the focal plane image and its contrast as a function of the Zernike coefficients applied to the segments. This analytical model requires then to be inverted to obtain the upper constraints in cophasing and stability that need to be respected to achieve the desired contrast. In this paper, we focus only on the development of the analytical model and on its validation, the inversion of the model and its application to tolerancing being the studies of future work.
In Section 2, we introduce this analytical model, which is based on a perfect coronagraph to model high-contrast performance and a segment-based model of the pupil. In Section 3, we apply this model to a LUVOIR-like pupil. In particular, its outputs are compared to images issued from an end-to-end simulation, where the LUVOIR-like pupil is combined first with a perfect coronagraph, then with an Apodized Lyot Coronagraph (APLC) that enables a 10^{10} contrast in a circular dark hole from $4\lambda/D$ to $10\lambda/D$.

2. ANALYTICAL MODEL

This section aims at introducing and developing the formalism needed for the analytical model.

2.1 Pupil model

To make the variable use easier, we define $\vec{r}$ the position vector in the pupil plane and $\vec{u}$ the one in the detector plane (focal plane). The upstream pupil of the system is called P and is made of identical segments of generic shape S. The pupil is defined as follow:

$$P(\vec{r}) = \sum_{k=1}^{n_{seg}} S(\vec{r} - \vec{r_k}) \tag{1}$$

where, as shown in Fig. 1, $\vec{r_k}$ stands for the position vector pointing from the center of the central obstruction to the center of the segment number k. n_{seg} corresponds to the number of segments ($n_{seg} = 36$ for this LUVOIR-like pupil).

2.2 Phase aberration model

The phase aberration, called ϕ, can be expressed as the sum of a global phase aberration and local phase aberrations on the different segments:

$$\phi(\vec{r}) = \sum_{l=0}^{n_{zer}} a_l Z_{g,l}(\vec{r}) + \sum_{(k,l)=(1,0)}^{(n_{seg},n_{zer})} a_{k,l} S(\vec{r} - \vec{r_k}) \times Z_l(\vec{r} - \vec{r_k}) \tag{2}$$

where $(Z_{g,l})_{l\in[0,n_{zer}]}$ corresponds to the Zernike basis on the entire pupil and $(Z_l)_{l\in[0,n_{zer}]}$ corresponds to the Zernike basis on one segment.
Thanks to the telescope alignment and a first cophasing of the primary mirror, the main global and local aberrations can be removed, so only residual aberrations are left. Furthermore, by segmenting the residual global aberrations on the pupil, they can be seen as local aberrations. Therefore, for the rest of this communication, only residual local aberrations are considered:

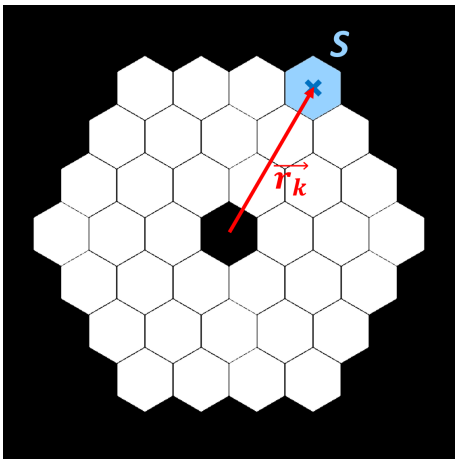

Figure 1. Definitions of the vectors $\vec{r_k}$ and of the shape of a generic segment S on a segmented pupil. In red, we can see the vector $\vec{r_{36}}$, from the center of the pupil to the 36th segment.

$$\phi(\vec{r}) = \sum_{(k,l)=(1,0)}^{(n_{seg},n_{zer})} a_{k,l} S(\vec{r} - \vec{r_k}) \times Z_l(\vec{r} - \vec{r_k}) \tag{3}$$

2.3 Imaging model

In case of phase aberration only, the electric field in the pupil plane can be expressed as:

$$E(\vec{r}) = P(\vec{r}) \times e^{i\phi(\vec{r})} \tag{4}$$

Since the aberrations are small, we get:

$$E(\vec{r}) = P(\vec{r}) \times (1 + i\phi(\vec{r})) \tag{5}$$

In the hypothesis of a perfect coronagraph, which is not realistic when the performance is limited by the coronagraph design, the amplitude of the electric field generated by the star can be removed,[17–19] which corresponds to the constant term 1 in the previous formula. Then, in the final detector plane, the amplitude of the electric field becomes:

$$E_f(\vec{u}) = i\widehat{P\phi}(\vec{u}) \tag{6}$$

where $\hat{f}$ is the Fourier Transform of the function f.

2.4 Imaging with phase aberration

By combining the equations 3 and 6, we obtain:

$$\begin{aligned} E_f(\vec{u}) &= i \sum_{(k,l)=(1,0)}^{(n_{seg},n_{zer})} a_{k,l} \widehat{(SZ_l)(\vec{r} - \vec{r_k})} \\ &= i \sum_{(k,l)=(1,0)}^{(n_{seg},n_{zer})} a_{k,l} \widehat{(SZ_l)}(\vec{u}) e^{-i\vec{r_k}.\vec{u}} \\ &= i \sum_{l=0}^{n_{zer}} \widehat{(SZ_l)}(\vec{u}) \sum_{k=1}^{n_{seg}} a_{k,l} e^{-i\vec{r_k}.\vec{u}} \end{aligned} \tag{7}$$

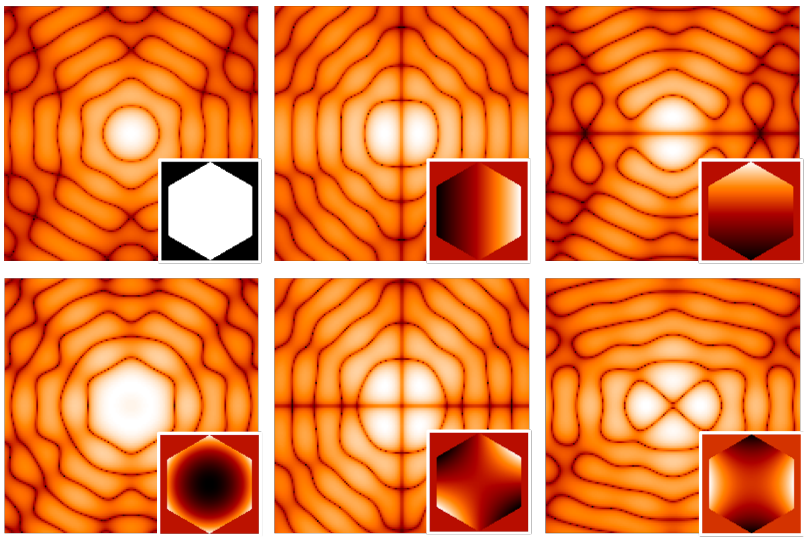

Figure 2. Envelopes corresponding to the first Zernikes. Top left: piston, top center: tip, top right: tilt, bottom left: focus, bottom center: 45° astigmatism, bottom right: 0° astigmatism. These envelopes will be multiplied to interference fringes between all the pairs of segments of the pupil.

Because $\widehat{(SZ_l)}(\vec{u})$ does not depend on k.

As we can see in this equation, every Zernike polynomial, Z_l, present on a segment acts on the final image plane as an envelope only, which does not depend on the segment positioning at all. Fig. 2 illustrates the envelopes for the first Zernikes.
The segments only indirectly act on the global coefficient of this envelope, $i\sum_{k=1}^{n_{seg}} a_{k,l}e^{-ir\vec{}_k.\vec{u}}$, which is influenced by the positions of the segments $r\vec{}_k$ and the local Zernike coefficients $a_{k,l}$.

2.5 Case of one single Zernike on the segments

In this case, only one Z_l is applied on the segments, even if they can still have different coefficients. The electric field in the image plane can then be expressed as:

$$E_f(\vec{u}) = i\widehat{SZ_l}(\vec{u}) \sum_{k=1}^{n_{seg}} a_{k,l} e^{-ir\vec{}_k.\vec{u}} \tag{8}$$

The intensity becomes:

$$\begin{aligned} I(\vec{u}) &= (i\widehat{SZ_l}(\vec{u}) \sum_{k=1}^{n_{seg}} a_{k,l} \exp(-ir\vec{}_k.\vec{u})) \times (-i\widehat{SZ_l}^*(\vec{u}) \sum_{k=1}^{n_{seg}} a_{k,l} \exp(ir\vec{}_k.\vec{u})) \\ &= \left\|\widehat{SZ_l}(\vec{u})\right\|^2 \sum_{k_1=1}^{n_{seg}} \sum_{k_2=1}^{n_{seg}} a_{k_1,l}a_{k_2,l} e^{i(r\vec{}_{k_2} - r\vec{}_{k_1}).\vec{u}} \end{aligned} \tag{9}$$

Since the intensity is real, $\sum_{k_1=1}^{n_{seg}} \sum_{k_2=1}^{n_{seg}} a_{k_1,l}a_{k_2,l} e^{i(r\vec{}_{k_2} - r\vec{}_{k_1}).\vec{u}}$ is real, and therefore:

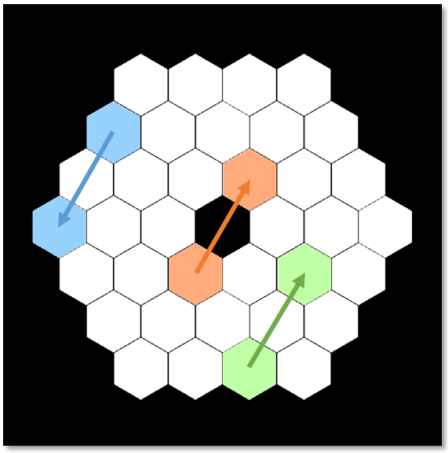

Figure 3. Illustration of some redundant oriented pairs that correspond to one single non-redundant pair. 42 oriented pairs generate exactly the same interference fringes than the pair $\vec{r_{16}} - \vec{r_{28}}$ (blue), for example the pairs $\vec{r_{25}} - \vec{r_{12}}$ (orange) and $\vec{r_{14}} - \vec{r_{3}}$ (green). Since these 42 pairs have the same effect in the detector plane, they can all be replaced by one single pair, called the non-redundant pair.

$$\begin{aligned} I(\vec{u}) &= \left\|\widehat{SZ_l}(\vec{u})\right\|^2 \times \Big(\sum_{k=1}^{n_{seg}} a_{k,l}^2 + \Re\Big(\sum_{k_1=1}^{n_{seg}} \sum_{k_2=1, k_2\neq k_1}^{n_{seg}} a_{k_1,l} a_{k_2,l} e^{i(\vec{r_{k_2}} - \vec{r_{k_1}}).\vec{u})} \\ &= \left\|\widehat{SZ_l}(\vec{u})\right\|^2 \times \Big(\sum_{k=1}^{n_{seg}} a_{k,l}^2 + \sum_{k_1=1}^{n_{seg}} \sum_{k_2=1, k_2\neq k_1}^{n_{seg}} a_{k_1,l} a_{k_2,l} \cos((\vec{r_{k_2}} - \vec{r_{k_1}}).\vec{u})\Big) \end{aligned} \tag{10}$$

It appears here that studying the effect of random values of the same Zernike on all the segments is equivalent to studying the interference effects on each pair of segments and summing them.
n_{NRP} represents the number of non-redundant segment pairs and $(\vec{b_q})_{q\in[1,n_{NRP}]}$ the basis of non-redundant segment pairs. In the case of the LUVOIR-like pupil, which contains 36 segments, there are 1260 possible oriented pairs of segments (obtained with the binomial coefficient $2 \times C_{36}^2$), but $n_{NRP} = 63$. In the case of JWST, there are 306 pairs of segments in total, but only 30 non-redundant pairs of segments. The Fig. 3 illustrates the redundancy of some pairs of segments.

Then we can write:

$$I(\vec{u}) = \left\|\widehat{SZ_l}(\vec{u})\right\|^2 \times \Big(\sum_{k=1}^{n_{seg}} a_{k,l}^2 + 2\sum_{q=1}^{n_{NRP}} A_q \cos(\vec{b_q}.\vec{u})\Big) \tag{11}$$

where, for $q \in [1, n_{NRP}]$, $A_q = \sum_{(k_1,k_2)} a_{k_1,l} a_{k_2,l}$ and the couples (k_1, k_2) are all the couples that verify the relation $\vec{r_{k_2}} - \vec{r_{k_1}} = \pm\vec{b_q}$.
We can conclude that it is possible to obtain a relation between the final image, a certain baseline, and the Zernike coefficients applied on each segment of the baseline.

3. APPLICATION TO THE LUVOIR GEOMETRY

In this section, we apply the analytical model previously developed to the LUVOIR-like pupil and compare the results given by the model to an end-to-end simulation designed to respect the high-contrast conditions.

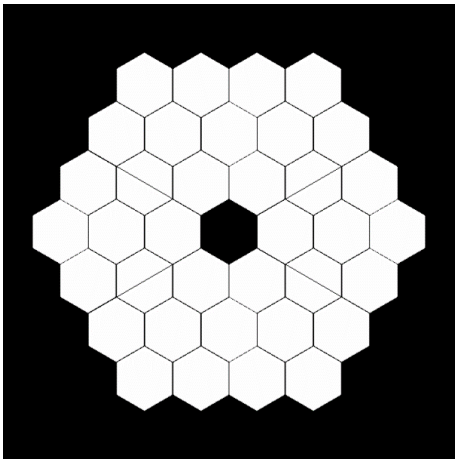

Figure 4. Pupil of a LUVOIR-like telescope, chosen for this study. It is made of 36 segments, a hexagonal central obstruction, and spiders.

3.1 Choice of pupil and end-to-end simulation

The LUVOIR-like pupil chosen for this study is formed of 36 identical hexagonal segments and a hexagonal central obstruction (see Fig. 4).[20,21]
In the following sections, we compare the outputs of the analytical model, exactly computed from the formula 13, and the outputs of the end-to-end simulation using the LUVOIR-like pupil. Two coronagraphs are used in the end-to-end simulation: a perfect coronagraph that fully removes the starlight,[17–19] and a realistic coronagraph, an APLC,[22–24] specially designed for the LUVOIR-like pupil to obtain a contrast higher than 10^{10} in the dark region, ie. between $4\lambda/D$ and $10\lambda/D$.
The APLC is a system of an Apodizer, located in a pupil plane, a Focal Plane Mask (FPM), in a focal plane, and a Lyot Stop, in a pupil plane (see Fig. 5). This configuration and the design of these different components enable to obtain an extremely high contrast in the dark hole, needed to image Earth-like planets (see Fig. 6). Since this area corresponds to the conditions of the theoretical model, we look at the images and performance in this area only and compare them to the outputs of the model. In our case, the interest region corresponds to a circular zone between $4\lambda/D$ and $10\lambda/D$.
Here we can derive the first difference between the results from the model and from the end-to-end simulation with an APLC: the contrast with no aberration in the first case is the absolute zero, and around 10^{10} in the second case. On the opposite, the end-to-end simulation with a perfect coronagraph also gives absolute zero.

3.2 Comparison between analytical model and end-to-end simulation for piston aberrations on the segments

Since the analytical model is based on the same theory than the perfect coronagraph with removal of the starlight (eq.5 to 6), we first compare the output from the end-to-end simulation with a perfect coronagraph and the output from the analytical model.
Two cases are compared here: case where two segments only are not well-phased, which should generate clear interference fringes and case where three segments are not well-phased. These configurations have been chosen since they generate clear patterns in the dark hole. The results are shown in the top two rows of Fig. 7. Obviously, there is a strong similarity between the PSF resulting from the end-to-end simulation and the one resulting from the analytical model. The rms values of these images are indicated in table 1 and confirm such a similitude between the two images. In Fig. 7, on the right, the cross sections of the two PSF on their 33rd rows are also plotted: they are similar to each other.

Now that the perfect coronagraph case has been verified, the analytical model is compared to a realistic coronagraph, the APLC described before. Like in the perfect coronagraph case, we begin with the two-segment

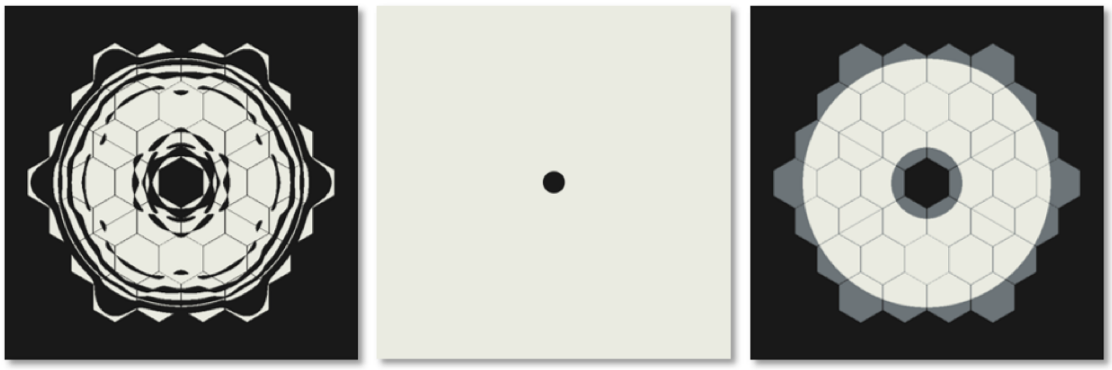

Figure 5. Optical masks used in the end-to-end simulation. The apodizer (left) is located in the first pupil plane, the focal plane mask (center) on the following focal plane, and the Lyot Stop (circular aperture on the right, here superposed with the entrance pupil) on the last pupil plane. Together, these three components form a so-called Apodized Lyot Coronagraph (APLC).

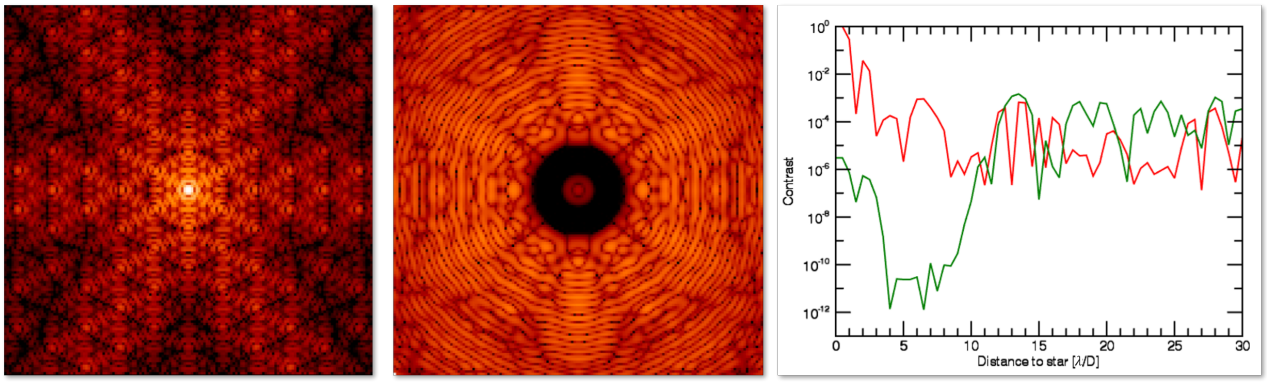

Figure 6. Left: PSF in presence of the LUVOIR-like pupil. Center: Same PSF, but in presence of the APLC. Right: Cut along a radius of the two previous PSF (red: without APLC, green: with APLC). We can observe that the APLC brings a huge correction in the interest region, ie. between $4\lambda/D$ and $10\lambda/D$.

Configuration	Method	RMS
Configuration 1	End-to-end simulation with perfect coronagraph	9.69×10^{-6}
	Analytical model	9.67×10^{-6}
Configuration 2	End-to-end simulation with perfect coronagraph	1.13×10^{-5}
	Analytical model	1.12×10^{-5}
Configuration 3	End-to-end simulation with APLC	3.24×10^{-6}
	Analytical model	4.12×10^{-6}
Configuration 4	End-to-end simulation with APLC	8.02×10^{-6}
	Analytical model	8.90×10^{-6}

Table 1. RMS values of the outputs from the end-to-end simulations and from the analytical model for four different configurations. Configuration 1 refers to the first lines of Fig. 7, Configuration 2 to the second line, Configuration 3 to the third line and Configuration 4 to the bottom line. Thanks to the normalisation, the outputs from both methods, in each configuration, have the same extrema.

and three-segment configurations. The results are illustrated in Fig. 7 and numerical values are given in table 1. Once again, we can see a very close similitude between the PSF issued from the analytical model, and the ones issued from the end-to-end simulation.

A phase is now generated with random piston aberrations from 0 to 15nm on the segments and propagated through two end-to-end simulations: one using the perfect coronagraph, one using the APLC. The same phase is applied in the analytical model. The phase and PSF are illustrated in Fig. 8. Once again, the images present the same patterns, even if the similitude is better between the analytical model and the propagation through a perfect coronagraph than between the analytical model and the propagation through the APLC.

A traditional error budget aims to quantify the deterioration of the contrast with the rms piston phase applied on the segments. To illustrate this effect, Fig. 9 indicates on the left the radial contrast as a function of the angular separation, in the dark hole only, for different rms piston values applied on the segments. These curves were only obtained using the analytical model and require further studies to be adjusted. We can recognize the characteristic shape of the piston envelope, which was shown in Fig. 2. The grey zone below 10^{10} is due to the limitation of a realistic coronagraph, which is not taken into account in the analytical model. The second plot in Fig. 9, also issued from the analytical model only, indicates the mean contrast in the dark region as a function of the rms piston values applied on the segments. This plot, once well-normalized, will quantify the actual constraints on piston cophasing of the segments, even if the formalism inversion mentioned in the introduction should give a faster and more accurate result, non-redundant-bases- and segment-dependant.

The application of the analytical model to piston aberrations on segments has been validated. In the next section, we generalize the application to other Zernikes.

3.3 Comparison between analytical model and end-to-end simulation for other aberrations

In this section, we compare the PSF and their cross-section at the 33rd row issued from the analytical model and the end-to-end simulation with an APLC, when tip, focus, and 0-astigmatism are applied on segments. The aberrations are only applied on one pair of segments, since the patterns are then really well-defined in the dark region.
Fig. 10 illustrates the results from this study. The envelopes are visible in Fig. 2, even if the scale does not match that of the PSF (150 pixels vs 40 pixels). In the tip case, the envelope creates a dark vertical line crossing the center of the PSF, which also appears in the PSF or the cross-sections at the top of Fig. 10. In the focus case, the envelope has a ring shape, which is also visible in the two PSF in the middle of Fig. 10. Finally, in the 0-astigmatism, the envelope has a bow-tie shape, which becomes a cross after being cut by the dark hole. This effect also clearly appears in the image issued from the end-to-end simulation.
These preliminary images show that the analytical model is still reliable when it comes to other Zernikes. The next step is a generalization of the model to a combination of Zernikes, to avoid studying them separately.

4. CONCLUSIONS

This paper aims at introducing an analytical model that is the basis of a new method for error budgets, both in static and dynamic modes. The formalism has been validated, using comparisons with both a perfect coronagraph and a realistic coronagraph. Its only limitation for now is the coronagraph: the analytical model takes into account a simplified model for the coronagraph, so adapting this formalism to a realistic coronagraph will probably add a calibration step in the process. For example, we know that the apodisation of the APLC does have an effect on the amplitudes of the interference fringes.
The next step of this study is a generalization of this analytical model to a combination of Zernikes. Then, the formula will be reversed to obtain this time the Zernike coefficients as a function of the desired contrast. This inversion method is based on the hypothesis that all the non-redundant baselines equally contribute to the final contrast deterioration. This process will enable a fast and complete error budget for any segmented pupil.
The static or quasi-static errors on the segments are not the only issue in high-contrast imaging. The telescope

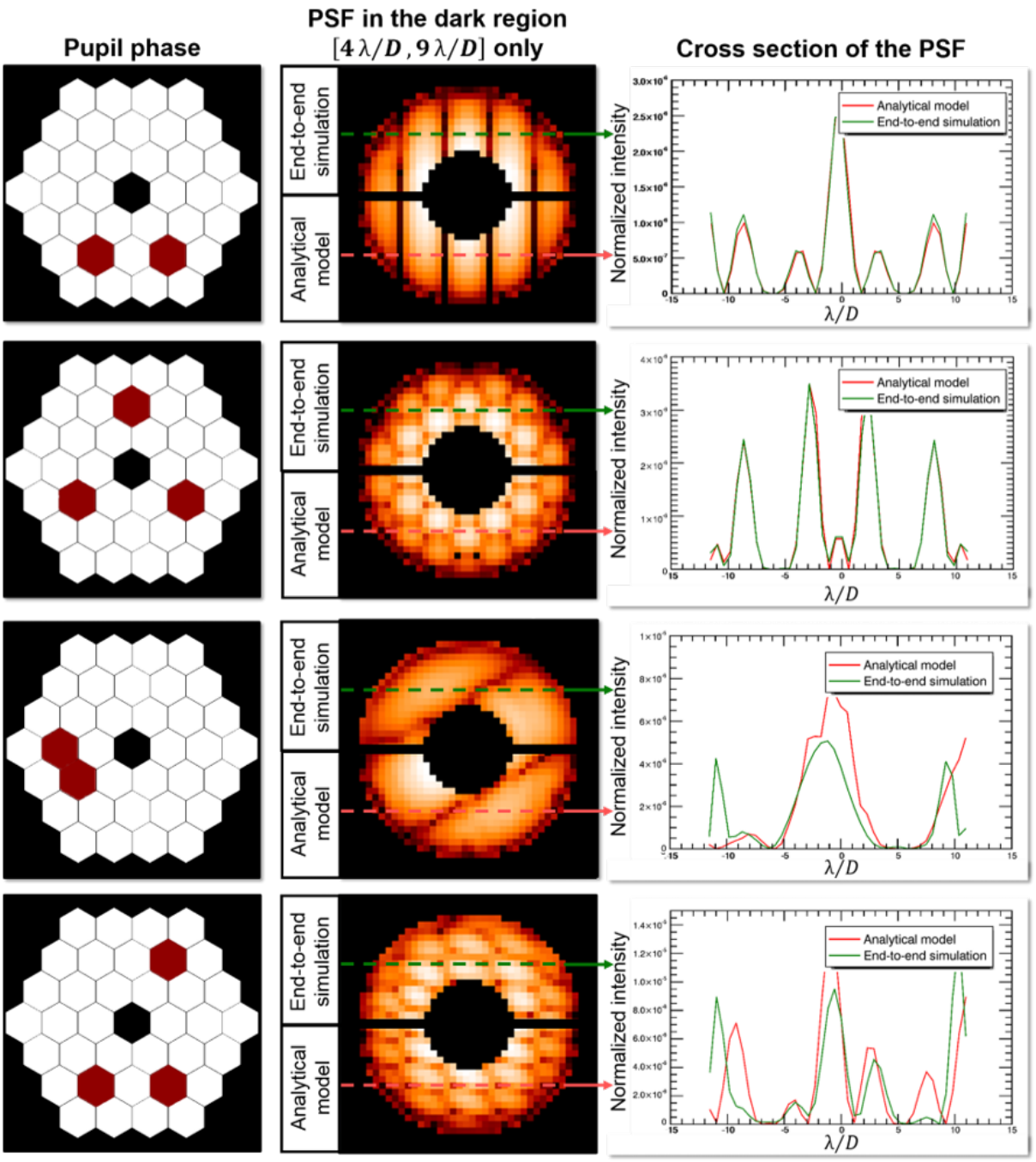

Figure 7. Results when identical piston values are applied on some segments of the pupil. Top two rows: comparison between the output from the end-to-end simulation with a perfect coronagraph and the output from the analytical model. Bottom two rows: comparison between the output from the end-to-end simulation with a realistic coronagraph (Apodized Lyot Coronagraph) and the output from the analytical model. On each row, left: phase applied on the pupil, where the white segments have no piston and the red segments have a 15nm piston applied on them. Center: Comparison of the PSF resulting from the end-to-end simulation and from the analytical model in the dark hole only. A central symmetry should be observed. Because of a small issue that has not been fixed yet, the amplitude of the analytical model output has been adjusted so its maximum fits the maximum of the end-to-end simulation PSF. Right: Cross section at the 33rd line of the end-to-end simulation and analytical model outputs.

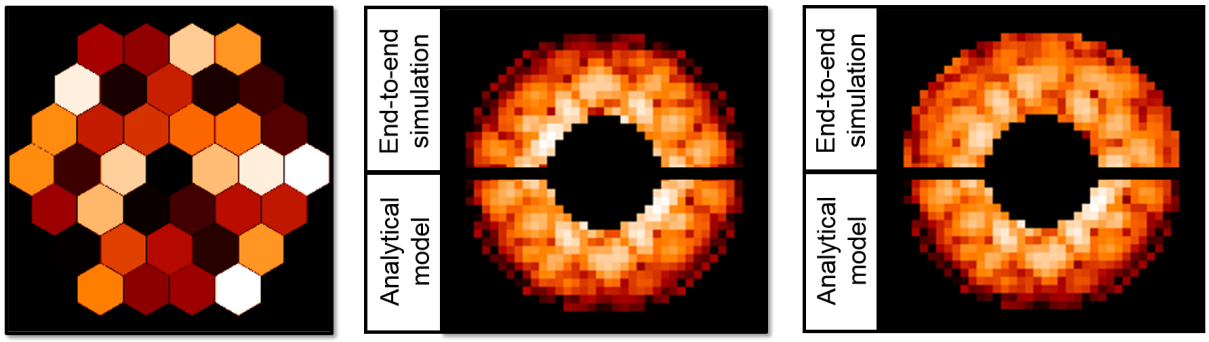

Figure 8. Results with the same random piston phase applied on the segmented pupil. Left: Phase applied on the segments. The piston coefficients are in the 0nm to 15nm range. Center: Combination of the PSF resulting from the end-to-end simulation in the perfect coronagraph case (top) and from the analytical model case (bottom). Right: Combination of the PSF resulting from the end-to-end simulation in the APLC case (top) and from the analytical model case (bottom). Once again, the amplitude of the analytical model output has been adjusted so its maximum fits the maximum of the end-to-end simulation PSF. A central symmetry should be observed.

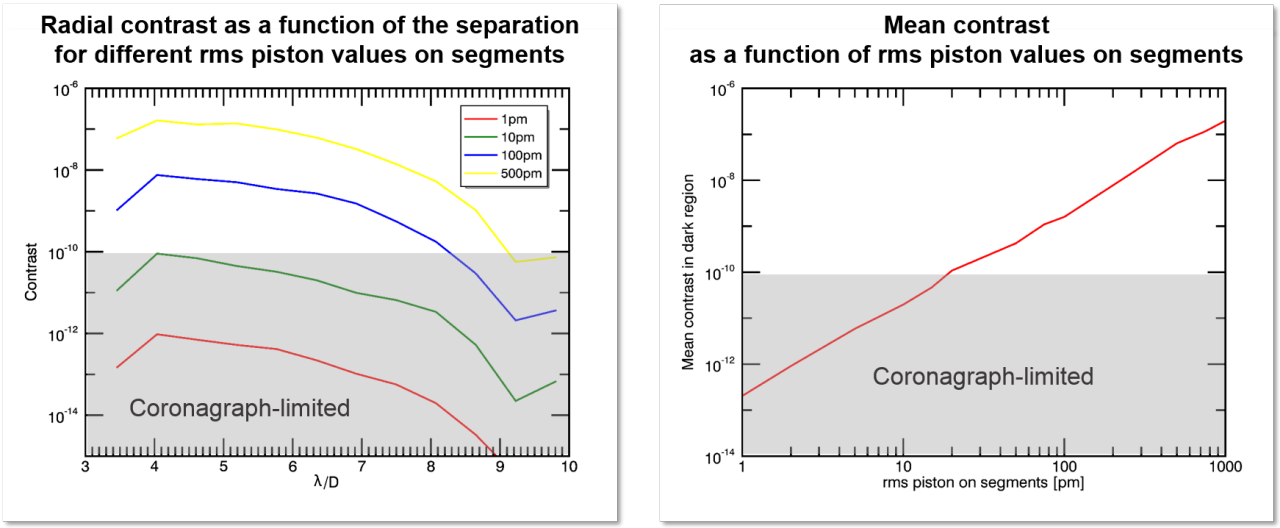

Figure 9. Results from the analytical model only. Left: Radial contrast as a function of the angular separation for different rms piston values applied on the segments. Right: Mean contrast in the dark region as a function of the rms piston values on the segments. In these two graphs, the grey zone corresponds to the performance limited by the coronagraph. Since the analytical model is based on a perfect coronagraph, it gives an absolute zero with no aberration, which is not realistic. The grey zone indicates where this artefact of the model appears.

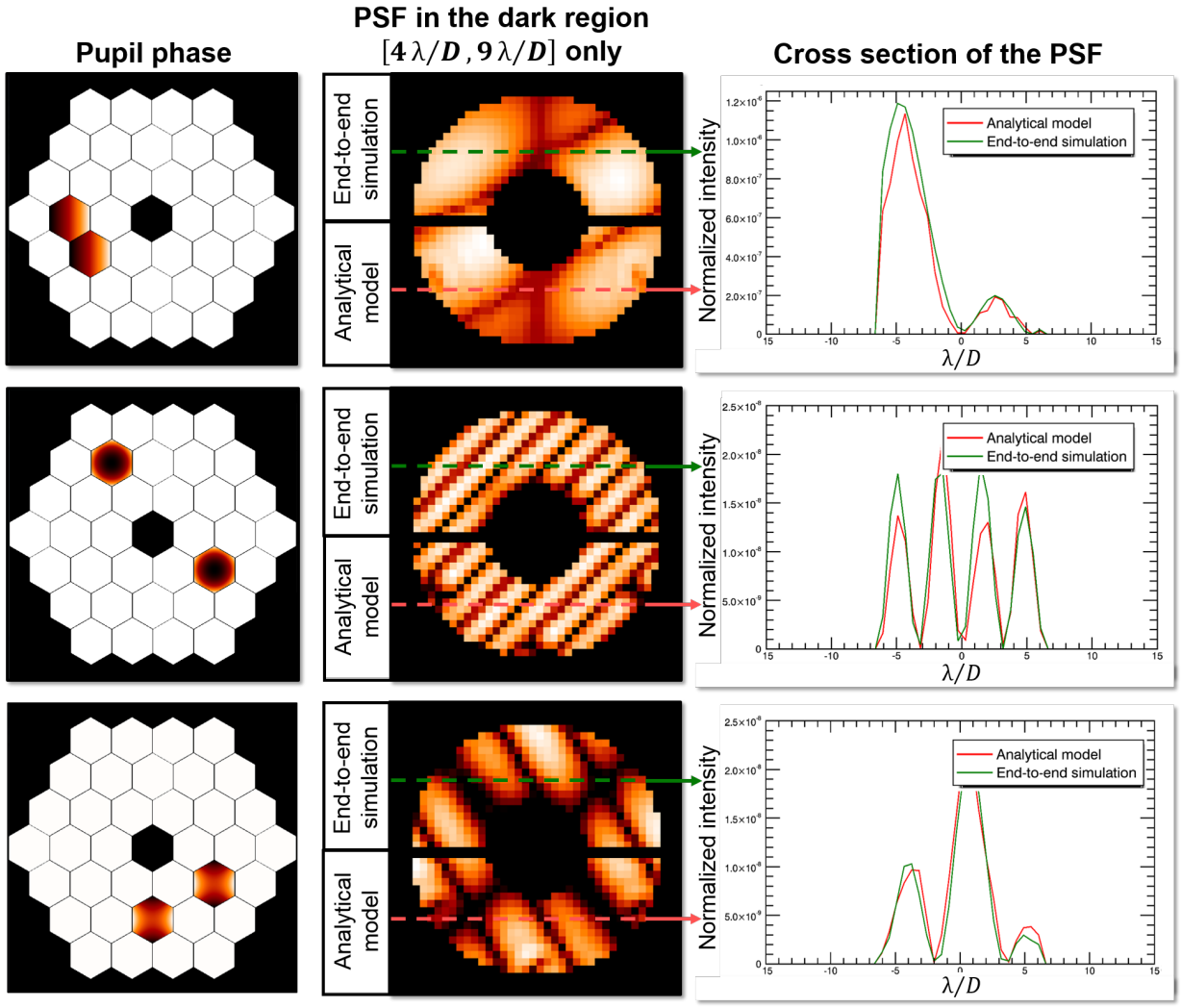

Figure 10. comparison between the output from the end-to-end simulation with an APLC and the output from the analytical model when identical Zernike coefficients are applied on one pair of segments. Top row: comparison when a tip is applied on two segments. Center row: comparison when a focus is applied on two segments. Bottom row: comparison when a 0-astigmatism is applied on two segments. On each row, left: phase applied on the pupil, where the white segments have no aberration. Center column: Comparison of the PSF resulting from the end-to-end simulation and from the analytical model in the dark hole only. A central symmetry should be observed. Because of a small issue that has not been fixed yet, the amplitude of the analytical model output has been adjusted so its maximum fits the maximum of the end-to-end simulation PSF. Right: Cross section at the 33rd line of the end-to-end simulation and analytical model outputs.

vibrations or the resonant modes of the segments also generate instability issues, which are important factors in the limitation of the performance. This formalism needs then to be applied on the dynamic case, where only the Zernike coefficients are time-dependant.
Such a new formalism to describe segmented pupils and generate images is very fast to compute. It is also adaptable to any segmented pupils, such as the Extremely Large Telescopes, the Thirty Meters Telescopes, the James Webb Space Telescope or the new HabEx and LUVOIR pupils. It can even been applied to non-hexagonal-segment pupils, such as the Giant Magellan Telescope. Such an analytical model enables a new, fast, and efficient method in static error budget and stability analysis for all segmented telescopes.

ACKNOWLEDGMENTS

This work is supported in part by the National Aeronautics and Space Administration under Grants NNX12AG05G and NNX14AD33G issued through the Astrophysics Research and Analysis (APRA) program (PI: R. Soummer) and by Jet Propulsion Laboratory subcontract No.1539872 (Segmented-Aperture Coronagraph Design and Analysis; PI: R. Soummer).
It is also partly funded by the French Aerospace Lab (ONERA) in the frame of the VASCO Research Project and by the Laboratoire d'Astrophysique de Marseille (LAM).

REFERENCES

1. D. Spergel, N. Gehrels, C. Baltay, D. Bennett, J. Breckinridge, M. Donahue, A. Dressler, B. S. Gaudi, T. Greene, O. Guyon, C. Hirata, J. Kalirai, N. J. Kasdin, B. Macintosh, W. Moos, S. Perlmutter, M. Postman, B. Rauscher, J. Rhodes, Y. Wang, D. Weinberg, D. Benford, M. Hudson, W.-S. Jeong, Y. Mellier, W. Traub, T. Yamada, P. Capak, J. Colbert, D. Masters, M. Penny, D. Savransky, D. Stern, N. Zimmerman, R. Barry, L. Bartusek, K. Carpenter, E. Cheng, D. Content, F. Dekens, R. Demers, K. Grady, C. Jackson, G. Kuan, J. Kruk, M. Melton, B. Nemati, B. Parvin, I. Poberezhskiy, C. Peddie, J. Ruffa, J. K. Wallace, A. Whipple, E. Wollack, and F. Zhao, "Wide-Field InfrarRed Survey Telescope-Astrophysics Focused Telescope Assets WFIRST-AFTA 2015 Report," *ArXiv e-prints* , Mar. 2015.
2. J. Dalcanton, S. Seager, S. Aigrain, S. Battel, N. Brandt, C. Conroy, L. Feinberg, S. Gezari, O. Guyon, W. Harris, C. Hirata, J. Mather, M. Postman, D. Redding, D. Schiminovich, H. P. Stahl, and J. Tumlinson, "From Cosmic Birth to Living Earths: The Future of UVOIR Space Astronomy," *ArXiv e-prints* , July 2015.
3. L. Pueyo, "The LUVOIR coronagraph instrument: definition and design," in *UV/Optical/IR Space Telescopes and Instruments: Innovative Technologies and Concepts VIII*, *SPIE paper 10398-15 in these proceedings*, 2017.
4. B. Mennesson, S. Gaudi, S. Seager, K. Cahoy, S. Domagal-Goldman, L. Feinberg, O. Guyon, J. Kasdin, C. Marois, D. Mawet, M. Tamura, D. Mouillet, T. Prusti, A. Quirrenbach, T. Robinson, L. Rogers, P. Scowen, R. Somerville, K. Stapelfeldt, D. Stern, M. Still, M. Turnbull, J. Booth, A. Kiessling, G. Kuan, and K. Warfield, "The Habitable Exoplanet (HabEx) Imaging Mission: preliminary science drivers and technical requirements," in *Space Telescopes and Instrumentation 2016: Optical, Infrared, and Millimeter Wave*, *Presented at the Society of Photo-Optical Instrumentation Engineers (SPIE) Conference* **9904**, p. 99040L, July 2016.
5. S. M. Adkins, I. S. McLean, M. P. Fitzgerald, J. E. Larkin, H. A. Lewis, C. Martin, D. Mawet, J. X. Prochaska, and P. Wizinowich, "New developments in instrumentation at the W. M. Keck Observatory," in *Ground-based and Airborne Instrumentation for Astronomy VI*, *Presented at the Society of Photo-Optical Instrumentation Engineers (SPIE) Conference* **9908**, p. 990805, Aug. 2016.
6. M. M. Colavita, P. L. Wizinowich, R. L. Akeson, S. Ragland, J. M. Woillez, R. Millan-Gabet, E. Serabyn, M. Abajian, D. S. Acton, E. Appleby, J. W. Beletic, C. A. Beichman, J. Bell, B. C. Berkey, J. Berlin, A. F. Boden, A. J. Booth, R. Boutell, F. H. Chaffee, D. Chan, J. Chin, J. Chock, R. Cohen, A. Cooper, S. L. Crawford, M. J. Creech-Eakman, W. Dahl, G. Eychaner, J. L. Fanson, C. Felizardo, J. I. Garcia-Gathright, J. T. Gathright, G. Hardy, H. Henderson, J. S. Herstein, M. Hess, E. E. Hovland, M. A. Hrynevych, E. Johansson, R. L. Johnson, J. Kelley, R. Kendrick, C. D. Koresko, P. Kurpis, D. Le Mignant, H. A. Lewis, E. R. Ligon, W. Lupton, D. McBride, D. W. Medeiros, B. P. Mennesson, J. D. Moore, D. Morrison,

C. Nance, C. Neyman, A. Niessner, C. G. Paine, D. L. Palmer, T. Panteleeva, M. Papin, B. Parvin, L. Reder, A. Rudeen, T. Saloga, A. Sargent, M. Shao, B. Smith, R. F. Smythe, P. Stomski, K. R. Summers, M. R. Swain, P. Swanson, R. Thompson, K. Tsubota, A. Tumminello, C. Tyau, G. T. van Belle, G. Vasisht, J. Vause, F. Vescelus, J. Walker, J. K. Wallace, U. Wehmeier, and E. Wetherell, "The Keck Interferometer," *Publications of the Astronomical Society of the Pacific* **125**, p. 1226, Oct. 2013.

7. B. Macintosh, M. Troy, R. Doyon, J. Graham, K. Baker, B. Bauman, C. Marois, D. Palmer, D. Phillion, L. Poyneer, I. Crossfield, P. Dumont, B. M. Levine, M. Shao, G. Serabyn, C. Shelton, G. Vasisht, J. K. Wallace, J.-F. Lavigne, P. Valee, N. Rowlands, K. Tam, and D. Hackett, "Extreme adaptive optics for the Thirty Meter Telescope," in *Society of Photo-Optical Instrumentation Engineers (SPIE) Conference Series*, *Presented at the Society of Photo-Optical Instrumentation Engineers (SPIE) Conference* **6272**, p. 62720N, June 2006.
8. M. E. Kasper, J.-L. Beuzit, C. Verinaud, N. Yaitskova, P. Baudoz, A. Boccaletti, R. G. Gratton, N. Hubin, F. Kerber, R. Roelfsema, H. M. Schmid, N. A. Thatte, K. Dohlen, M. Feldt, L. Venema, and S. Wolf, "EPICS: the exoplanet imager for the E-ELT," in *Adaptive Optics Systems*, *Presented at the Society of Photo-Optical Instrumentation Engineers (SPIE) Conference* **7015**, p. 70151S, July 2008.
9. R. Davies, N. Ageorges, L. Barl, L. R. Bedin, R. Bender, P. Bernardi, F. Chapron, Y. Clenet, A. Deep, E. Deul, M. Drost, F. Eisenhauer, R. Falomo, G. Fiorentino, N. M. Förster Schreiber, E. Gendron, R. Genzel, D. Gratadour, L. Greggio, F. Grupp, E. Held, T. Herbst, H.-J. Hess, Z. Hubert, K. Jahnke, K. Kuijken, D. Lutz, D. Magrin, B. Muschielok, R. Navarro, E. Noyola, T. Paumard, G. Piotto, R. Ragazzoni, A. Renzini, G. Rousset, H.-W. Rix, R. Saglia, L. Tacconi, M. Thiel, E. Tolstoy, S. Trippe, N. Tromp, E. A. Valentijn, G. Verdoes Kleijn, and M. Wegner, "MICADO: the E-ELT adaptive optics imaging camera," in *Ground-based and Airborne Instrumentation for Astronomy III*, *Presented at the Society of Photo-Optical Instrumentation Engineers (SPIE) Conference* **7735**, p. 77352A, July 2010.
10. S. P. Quanz, I. Crossfield, M. R. Meyer, E. Schmalzl, and J. Held, "Direct detection of exoplanets in the 3-10 μm range with E-ELT/METIS," *International Journal of Astrobiology* **14**, pp. 279–289, Apr. 2015.
11. J. T. Trauger and W. A. Traub, "A laboratory demonstration of the capability to image an Earth-like extrasolar planet," *Nature* **446**, pp. 771–773, Apr. 2007.
12. P. Baudoz, J. Mazoyer, M. Mas, R. Galicher, and G. Rousset, "Dark hole and planet detection: laboratory results using the self-coherent camera," in *Ground-based and Airborne Instrumentation for Astronomy IV*, *Presented at the Society of Photo-Optical Instrumentation Engineers (SPIE) Conference* **8446**, p. 84468C, Sept. 2012.
13. J. Mazoyer, P. Baudoz, R. Galicher, and G. Rousset, "High-contrast imaging in polychromatic light with the self-coherent camera," *Astronomy & Astrophysics* **564**, p. L1, Apr. 2014.
14. M. T. Stahl, "Effects of space telescope primary mirror segment errors on coronagraph instrument performance," in *UV/Optical/IR Space Telescopes and Instruments: Innovative Technologies and Concepts VIII*, *SPIE paper 10398-16 in these proceedings*, 2017.
15. M. A. Greenhouse, "The JWST science instrument payload: mission context and status," in *Space Telescopes and Instrumentation 2016: Optical, Infrared, and Millimeter Wave*, *Presented at the Society of Photo-Optical Instrumentation Engineers (SPIE) Conference* **9904**, p. 990406, July 2016.
16. M. Clampin, "Status of the James Webb Space Telescope (JWST)," in *SPIE*, **7010**, Aug. 2008.
17. F. Malbet, J. W. Yu, and M. Shao, "High-Dynamic-Range Imaging Using a Deformable Mirror for Space Coronography," *Publications of the Astronomical Society of the Pacific* **107**, p. 386, Apr. 1995.
18. A. Quirrenbach, "Coronographic Methods for the Detection of Terrestrial Planets," *ArXiv Astrophysics e-prints* , Feb. 2005.
19. C. Cavarroc, A. Boccaletti, P. Baudoz, T. Fusco, and D. Rouan, "Fundamental limitations on Earth-like planet detection with extremely large telescopes," *Astronomy & Astrophysics* **447**, pp. 397–403, Feb. 2006.
20. M. Postman, T. Brown, K. Sembach, M. Giavalisco, W. Traub, K. Stapelfeldt, D. Calzetti, W. Oegerle, R. Michael Rich, H. Phillip Stahl, J. Tumlinson, M. Mountain, R. Soummer, and T. Hyde, "Advanced Technology Large-Aperture Space Telescope: science drivers and technology developments," *Optical Engineering* **51**, pp. 011007–011007, Jan. 2012.

21. L. D. Feinberg, A. Jones, G. Mosier, N. Rioux, D. Redding, and M. Kienlen, "A cost-effective and serviceable ATLAST 9.2m telescope architecture," in *Space Telescopes and Instrumentation 2014: Optical, Infrared, and Millimeter Wave*, *Presented at the Society of Photo-Optical Instrumentation Engineers (SPIE) Conference* **9143**, p. 914316, Aug. 2014.
22. R. Soummer, C. Aime, and P. E. Falloon, "Stellar coronagraphy with prolate apodized circular apertures," *Astronomy & Astrophysics* **397**, pp. 1161–1172, Jan. 2003.
23. M. N'Diaye, L. Pueyo, and R. Soummer, "Apodized Pupil Lyot Coronagraphs for Arbitrary Apertures. IV. Reduced Inner Working Angle and Increased Robustness to Low-order Aberrations," *Astrophysical Journal* **799**, p. 225, Feb. 2015.
24. M. N'Diaye, R. Soummer, L. Pueyo, A. Carlotti, C. C. Stark, and M. D. Perrin, "Apodized Pupil Lyot Coronagraphs for Arbitrary Apertures. V. Hybrid Shaped Pupil Designs for Imaging Earth-like planets with Future Space Observatories," *Astrophysical Journal* **818**, p. 163, Feb. 2016.